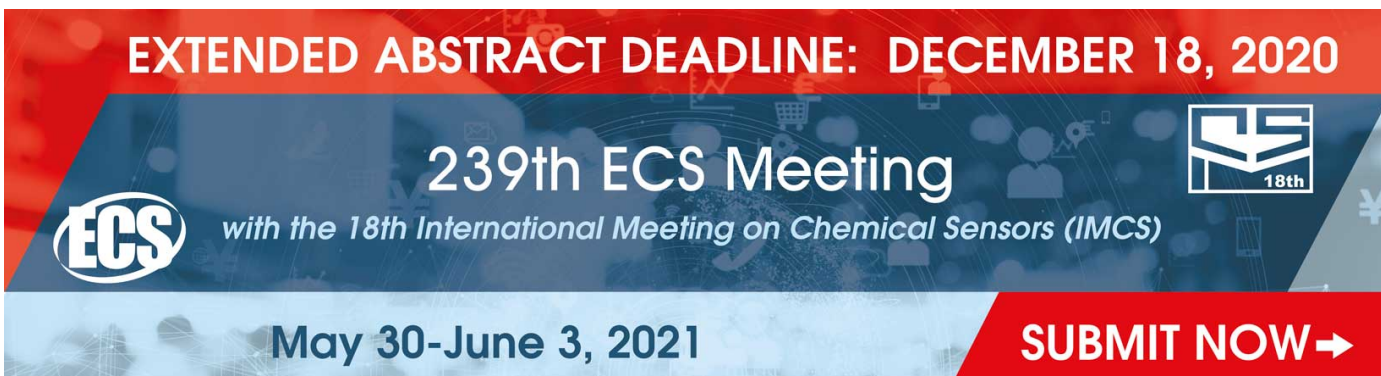


PAPER

## Controlling and optimizing the morphology and microstructure of 3D interconnected activated carbons for high performance supercapacitors

To cite this article: Yanhong Lu *et al* 2021 *Nanotechnology* **32** 085401

View the [article online](#) for updates and enhancements.

A promotional banner for the 239th ECS Meeting. The banner has a red top section with white text, a blue middle section with white and red text, and a red bottom right corner with white text. The background of the blue section features a network of nodes and lines, along with various scientific icons like a beaker, a magnifying glass, and a person. The ECS logo is on the left, and a stylized 'ECS' logo with '18th' is on the right.

**EXTENDED ABSTRACT DEADLINE: DECEMBER 18, 2020**

**239th ECS Meeting**  
with the 18th International Meeting on Chemical Sensors (IMCS)

**May 30-June 3, 2021**

**SUBMIT NOW →**

# Controlling and optimizing the morphology and microstructure of 3D interconnected activated carbons for high performance supercapacitors

Yanhong Lu<sup>1,\*</sup>, Suling Zhang<sup>1</sup>, Xiaorong Han<sup>1</sup>, Xingchen Wan<sup>1</sup>, Junlin Gao<sup>1</sup>, Congcong Bai<sup>1</sup>, Yingxue Li<sup>1</sup>, Zhen Ge<sup>2</sup>, Lei Wei<sup>1</sup>, Yu Chen<sup>1</sup>, Yanfeng Ma<sup>2</sup> and Yongsheng Chen<sup>2,\*</sup>

<sup>1</sup> School of Chemistry & Material Science, Langfang Normal University, Langfang, 065000, People's Republic of China

<sup>2</sup> The Centre of Nanoscale Science and Technology and Key Laboratory of Functional Polymer Materials, State Key Laboratory and Institute of Elemento-Organic Chemistry, College of Chemistry, Nankai University, Tianjin, 300071, People's Republic of China

E-mail: [luyanhong@lfnu.edu.cn](mailto:luyanhong@lfnu.edu.cn) and [yschen99@nankai.edu.cn](mailto:yschen99@nankai.edu.cn)

Received 27 August 2020, revised 23 October 2020

Accepted for publication 11 November 2020

Published 1 December 2020



## Abstract

For an active electrode material, the morphology, microstructure and the effective specific surface area derived from them, have a dominant effect for the high performance supercapacitors. In this study, 3D interconnected activated carbons with controlled and optimized morphologies and porous structures were prepared from accessible carbon source and graphene oxide by a hydrothermal carbonization and following an activation method. Through optimizing the ratios of the precursors and reaction conditions, an electrode material with excellent specific surface area of  $2318 \text{ m}^2 \text{ g}^{-1}$ , meso-/macro-pore ratio of 63.2% (meso-/macro-pore volume reached to  $0.83 \text{ cm}^3 \text{ g}^{-1}$ ), as well as an outstanding electrical conductivity of  $46.6 \text{ S m}^{-1}$ , was obtained. The materials exhibit superior double-layer capacitive performances on a symmetric supercapacitor, delivering superior specific capacitance of  $157 \text{ F g}^{-1}$  in organic electrolyte system at current density of  $0.5 \text{ A g}^{-1}$ , excellent energy density of  $37.6 \text{ Wh kg}^{-1}$  with a power density of  $7.1 \text{ kW kg}^{-1}$  and good cycling stability of capacitance retention of 94% over 7000 cycles. These results offer a practical method to prepare the desired carbon electrode materials with controlled morphology and structure for high efficiency electrochemical energy storage devices.

Supplementary material for this article is available [online](#)

Keywords: 3D carbon, graphene, morphology, microstructure, supercapacitor

(Some figures may appear in colour only in the online journal)

## 1. Introduction

Based on the excellent charge–discharge properties, high power density and long lifetime, supercapacitors (SCs) are

attracting tremendous attentions together with other various energy storage devices [1, 2]. As one type of SCs, electrochemical double-layer capacitors (EDLCs), which store energy depending on the electrolyte ion fast adsorption and desorption at the electrode material/electrolyte interface under an applied voltage, have been used as a very promising

\* Authors to whom any correspondence should be addressed.

energy device because of its improved cycling stability, superior reversibility and enhanced economic applicability [3–6]. Activated carbons (ACs) are considered to be the most promising materials as commercial electrodes of EDLCs owing to its outstanding specific surface area (SSA) and rich porous structures, which are beneficial to the adsorption and desorption of the electrolyte ions, and sequentially easily forming the electrical double layers [7–11]. However, the performance of most commercial ACs based electrode materials is still far from the requirements of practical applications and theoretical prediction in terms of the limitation of high effective SSA (not total SSA) [12–14], low electrical conductivity and kinetic behavior of electrolyte ion transport in tortuous porosity at high current rate [15, 16]. Considering the charge storage mechanism of EDLCs, the ability of storing charges of the ACs are directly depended on the effective SSA of the active electrode material [12, 13, 17, 18], not the total SSA, and thus an optimal electrode material of EDLC should possess a combination of high SSA and appropriate pore size distribution (PSD). Based on previous studies, the mesopores are the main contributors for the active sites for electrolyte ions, especially for the large size ions, such as ionic liquid and organic electrolyte systems [12, 13, 19, 20]. The macropores can be served as electron reservoirs for shortening ion transport and diffusion pathways during electrochemical processes [18, 21, 22]. Therefore, it is crucial to design and prepare the active electrode materials with high effective SSA (not the total SSA), abundant meso-/macro-pores and fully structural interconnectivity for high performance EDLC, which could be achieved by controlling their morphologies and microstructures. Unfortunately, less attentions have been given for this part compared with that on the total SSA of the materials. Also, in most of the related literatures for the ACs [23–26], the same token has been applied, with much less works have been focused on the control of morphologies and PSD with high meso-/macro-pore ratio. Furthermore, the impact of low electrical conductivity of such ACs is missing some attention too, as pristine/conventional ACs always show limited conductivity due to its amorphous/disordered structures [15].

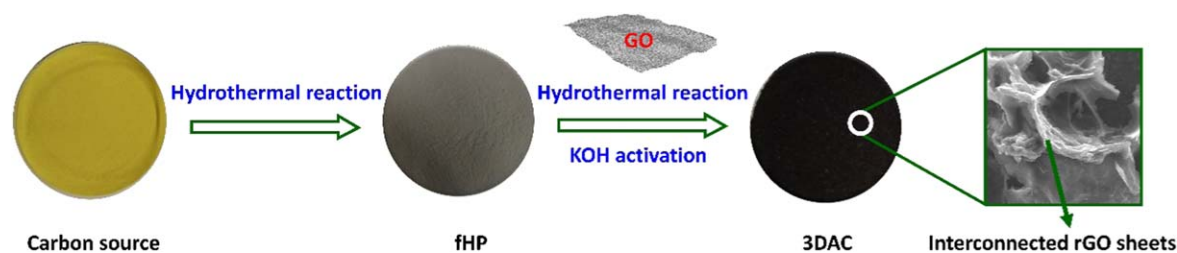
In this work, using an easily accessible carbon source together with a small amount of 2D carbon material of graphene oxide (GO) as precursors, a 3D interconnected porous activated carbons (3DAC) with controlled morphology, microstructure and effective SSA as well as large proportion of meso-/macro-pore was obtained using the standard industry hydrothermal carbonization and activation process. The 3D architecture not only prohibit the stacking of the carbon domains and thus leading to a high SSA and abundant meso-/macro-pores for the transport of the electrolyte ions, but also maintain the nature and intrinsic properties of individual graphene sheets, such as the excellent electron transport properties [27–29]. Compared with the conventional directly hydrothermal and carbonization method, this 3D interconnected meso-/macro-pore dominant carbon material prepared through optimizing the ration of precursors, with a mass ratio of 20 to 1 of carbon source derived hydrothermal product and GO, exhibits a superior SSA of  $2318\text{ m}^2\text{ g}^{-1}$ ,

meso-/macro-pore ratio of 63.2% and satisfied electrical conductivity of  $46.6\text{ S m}^{-1}$ . With above combined characteristics, 3DAC delivers a significant and important improved electrochemical performance using as the active electrode material for EDLCs, delivering an excellent specific capacitance value of  $157\text{ F g}^{-1}$  in organic electrolyte at the current density of  $0.5\text{ A g}^{-1}$ , superior charge and discharge process at the current density range of  $0.5\text{--}10\text{ A g}^{-1}$  and excellent cycling stability after 7000 cycles (94% retention). All the outstanding electrochemical performance have benefited from the favorable 3D interconnected morphologies with both high but controlled SSA and dominant meso-/macro-pores, which not only provide abundant ion accessible/adsorption sites for high capacitance but also offer facilitated channels to faster transportation and diffusion of electrolyte ions to high rate performance.

## 2. Experimental

### 2.1. Materials synthesis

GO was prepared through a modified Hummer's method according to our reported works [30, 31]. The commercial pollen pini was purchased from Jilin Hunchun Superior Products Co., Ltd. Before used, the pollen pini was dried for 12 h at  $120\text{ }^{\circ}\text{C}$  in vacuum. The 3DAC was prepared using a hydrothermal carbonization procedure and sequential activation process based on our reported methodes [13, 18]. Typically, pollen pini powder (8.00 g) was firstly dispersed in the distilled water (60 ml). After stirring at room temperature for 2 h, the suspension liquid was put into an autoclave (100 ml) and heated to  $180\text{ }^{\circ}\text{C}$  and kept for 12 h. The hydrothermal products were filtered, followed by washing and then drying at  $120\text{ }^{\circ}\text{C}$  in vacuum for 12 h. After grinding, a dark brown powder was obtained. These first hydrothermal products, named as fHP, were re-dispersed into distilled water, and mixed with GO suspension from the smallest to largest additive amount at the different weight ratio of 30:1, 25:1, 20:1 and 15:1, respectively. The as-prepared mixture was then conducted by the second hydrothermal process at  $120\text{ }^{\circ}\text{C}$  for 12 h, following the first hydrothermal and dried procedures. The second hydrothermal products, named as sHP-30, sHP-25, sHP-20 and sHP-15 according to the ratio of fHP and GO with 30:1, 25:1, 20:1 and 15:1, was mixed with KOH activation agent with four times weight. According to our earlier works [12, 13], the activation temperature of  $800\text{ }^{\circ}\text{C}\text{--}900\text{ }^{\circ}\text{C}$  was optimized. Therefore, the above homogeneous mixture was activated at  $800\text{ }^{\circ}\text{C}$  for 2 h in a horizontal tube furnace with a heating rate of  $5\text{ }^{\circ}\text{C min}^{-1}$  under Ar. The activation product was then washed with HCl (0.1 M) and distilled water until pH reached to  $\sim 7$ . The final products were dried at  $120\text{ }^{\circ}\text{C}$  in vacuum for 12 h, and named as 3DAC-15, 3DAC-20, 3DAC-25 and 3DAC-30, respectively. A control sample without GO was prepared using the same prepared method and was named as 3DAC-0.



**Scheme 1.** Schematic for the preparation process of 3DAC materials.

## 2.2. Characterization

The SSA was examined on a Micromeritics apparatus (ASAP 2020) at a test temperature of 77 K. The SSA and PSD analysis were performed using Brunauer–Emmett–Teller (BET) and non-local density functional theory method, respectively. Scanning electron microscopy (SEM) analysis was conducted to examine the surface morphology of materials on a Phenom Pro SEM. For microstructure analysis, high resolution transmission electron microscopy (HR-TEM) was performed on FEI Tecnai G2 F20 model electron microscope with 200 kV acceleration voltage. Raman spectra were analyzed with a spectrometer of LabRAM HR, and laser excitation wavelength of 514.5 nm was selected.  $I_D/I_G$  was nominated as the intensity ratio of D and G band. Lorentzian fitting was used to calculate the position and full-width half-maximum (FWHM) of D and G peaks. According to  $L_a = (560/E^4)(I_D/I_G)^{-1}$ , the mean size of carbon domains ( $L_a$ , nm) was obtained. Here,  $E$  is the laser energy with the value of 2.41 eV,  $I_D$  and  $I_G$  stands for the FWHM of the D and G bands, respectively. The crystalline phase studies of 3DAC materials were performed by x-ray diffraction (XRD, D/Max-2500, Rigaku) equipped with Cu K $\alpha$  radiation. The basal plane interlayer distance ( $d$ ) was calculated according to the equation of  $n\lambda = 2d \sin \theta$  based on the (002) diffraction peak ( $\lambda$  is the wavelength,  $\theta$  is the Bragg angle). The height of stacking carbon domains ( $L_c$ ) was carried out from (002) peak based on Scherrer's equation,  $L_c = K\lambda/(\beta_c \times \cos \theta)$ , where, the parameters of  $K$ ,  $\lambda$ ,  $\beta_c$  and  $\theta$  represent the shape factor (0.89), wavelength, FWHM and Bragg angle, respectively [15, 18]. X-ray photoelectron spectroscopy (XPS) analysis was determined using a Kratos Analytical spectrometer (AXIS HIS 165) with monochromator and Al K $\alpha$  radiation).

## 2.3. Fabrication of SCs

The symmetrical two-electrode SC devices were fabricated with 3DAC as electrode materials according to our previous reported methods [32, 33]. Typically, 3DAC materials were mixed with conductive carbon and polytetrafluoroethylene at the weight ratio of 85:5:10. The mixture was then grinded with a small amount of ethanol and subsequently rolled into a sheet with the thickness of 80–120  $\mu\text{m}$ . After punching into a circle shape with a diameter of 12 mm and dried at 120  $^\circ\text{C}$  in vacuum for 6 h, the electrode slices were matched weight and then pressed onto the hot carbon coated aluminum foils. The electrode slides were continued to be dried at 180  $^\circ\text{C}$  for 6 h under vacuum. Finally, the symmetrical 2032 coin-type

capacitors were assembled in an inert atmosphere glove box. The device consists of two electrodes separated by a cellulose film (TF4030, NKK), which are immersed in an organic electrolyte of 1.0 M tetraethylammonium tetrafluoroborate salt in acetonitrile (TEABF $_4$ /AN, Novolyte Co. Ltd).

## 2.4. Electrochemical measurements

The cyclic voltammetry (CV), along with the galvanostatic charge–discharge tests were studied on an electrochemical analyzer (CHI660C, Shanghai Chenhua) and a battery test system (CT2001A, Wuhan LAND) respectively. The voltage range of 0–2.7 V was selected. The electrochemical impedance spectroscopy (EIS) measurements were studied on the electrochemical workstation (Princeton P4000, USA) from 100 kHz to 10 mHz. The specific capacitance  $C_s$  (F g $^{-1}$ ), specific energy density ( $E$ , W h kg $^{-1}$ ) and specific power density ( $P$ , W kg $^{-1}$ ) of the symmetric SC devices, as well as the conductivity of 3DAC materials were tested and calculated according to our previous reported methods [18, 33–35].

# 3. Results and discussion

## 3.1. Structure and morphology characterization

As discussed above, introduction of GO in the raw materials, a 3D cross-linked and meso-/macropore dominant porous carbon material was designed and prepared through engineering the ratios of fHP and GO in the second hydrothermal carbonization and activation process. After hydrothermal and high temperature annealing in Ar, reduced graphene oxide (rGO) sheets will be formed [36]. As shown in scheme 1, these 2D rGO sheets would construct a 3D cross-linked carbon skeleton through addition GO precursor in the second hydrothermal process, and thereby a whole interconnected framework could be formed with these rGO sheets supported amorphous carbon domains, as will be discussed in details below. Through controlling and optimizing the additive amount of GO and the conditions of hydrothermal reaction as well as the activated process, 3DAC material with high effective SSA and optimized microstructure was obtained. Benefitting from their unique structure, the prepared 3DAC materials can deliver improved capacitive performance for SCs.

The microstructures including SSA and PSD of the series of 3DAC materials with different additive amount of GO were firstly investigated by nitrogen adsorption–desorption



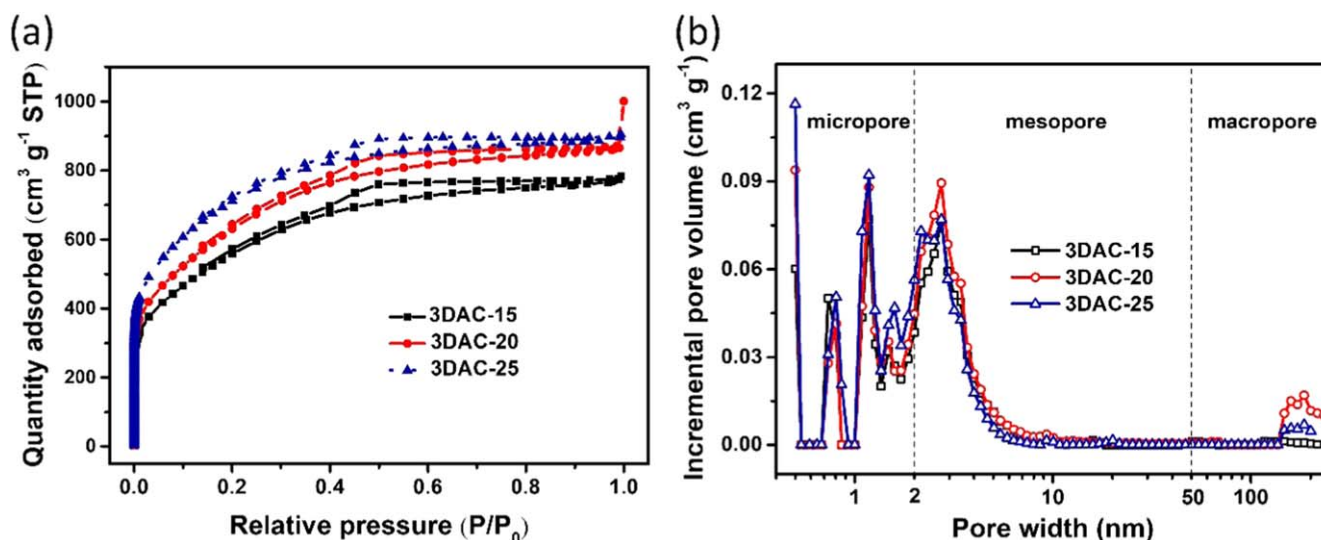


Figure 1. (a) Nitrogen adsorption–desorption isotherms. (b) PSD analysis of series of 3DAC materials.

isotherms. As shown in figure 1(a), the typical type-IV curves of 3DAC materials were exhibited, indicating of the major meso-porous structures [37]. The PSD analysis, as shown in figure 1(b), demonstrated the porous structures including micro-, meso- and macro- pores of the materials.

The SSA and PSD data for these samples with different GO loading deserve a careful analysis, as the loading has significant impact on SSA and PSD results, indicating probably morphology control/change. As shown in table 1, 3DAC-25 sample, with the lowest GO content, delivered the highest BET SSA of 2580 m<sup>2</sup> g<sup>-1</sup>. However, its PSD illustrated that most pores were micropores and the ratio of meso-/macro-pores was only 49.4%, which would not be favorable for fast electrolyte ion transport and diffusion [38]. With increased GO content, the meso-/macro-pore volume ratios were significantly increased. For 3DAC-20, the meso-/macro-pore ratio reached to 63.2%, corresponding to the increased mesopore and macropore volume to 0.68 and 0.15 cm<sup>3</sup> g<sup>-1</sup> respectively, as well as the highest total pore volume of 1.32 cm<sup>3</sup> g<sup>-1</sup>. Such unique microstructures contribute to a high effective/accessible SSA for electrolyte ions. With further increasing of the GO content, for the 3DAC-15 sample, the SSA was found to decrease to 2044 m<sup>2</sup> g<sup>-1</sup>, corresponding to the lowest total pore volume of 1.03 cm<sup>3</sup> g<sup>-1</sup>, which may be attributed to the overlap of the graphene sheets and the collapse of partial pore structure owing to the more GO content [38]. The above analysis results demonstrate that the microstructures of 3DAC strongly relies on the additive amount of GO precursors. Thus, the optimum microstructure of the ACs can be obtained through selecting the raw materials and controlling the ratios of the precursors at the optimized reaction conditions.

The above PSD analysis indicates that the 3DAC-20 sample has a meso-/macro-pore domination structure, which can contribute to the high accessible SSA and fast kinetic behavior of electrolyte ions and thus improve the 3DAC performance for electrode materials. Moreover, the introduction of GO can also lead to a relatively higher electrical

conductivity as observed before [21]. As shown in table 1, with the increasing of GO content, the electrical conductivity was correspondingly increased. For 3DAC-20 sample, although it did not manifest the best conductivity, it also showed obviously higher value than that of the control sample of 3DAC-25 (40.4 S m<sup>-1</sup>) and 3DAC-0 (35.3 S m<sup>-1</sup>). Such superior electrical conductivity of these electrode materials can contribute to a better electrochemical performance for SCs, such as rate performance and cycling stability.

The 3DAC materials appear as powder solid on the macroscopic morphology, as shown in the optical photos in figure S1 (available online at [stacks.iop.org/NANO/32/085401/mmedia](https://stacks.iop.org/NANO/32/085401/mmedia)). The microscopic morphology analysis of the series of 3DAC samples were evaluated by SEM and TEM. From the SEM images in figure 2, compared with the bulk agglomerate structures of 3DAC-0 (figures 2(a) and (b)), the irregular interconnected porous structures of 3DAC-15, 3DAC-20 and 3DAC-25 samples (figures 2(c)–(h)) were exhibited, which may be attributed to the contribution of rGO sheets [15]. Especially for 3DAC-20, the magnified SEM images in figures 2(d) and S2 showed the skeleton structure constructed by rGO sheets which has been loaded surrounding AC domains formed in the hydrothermal carbonization process. This looks like a reinforced concrete structure, where rGO sheets work as the template and form a 3D interconnected structure through cross-linking, and AC particles were deposited on the graphene sheets. Such a porous 3D structure not only offer enough macropores working as the electrolyte ion storage reservoir and are beneficial for the transport and diffusion, but also possess abundant mesopores favorable for electron ion adsorption.

The TEM images further highlighted the structures of the 3DAC materials. For 3DAC-0 material, an aggregated block morphology (figure 2(i)), along with a porous microstructure (figure 2(j)) were displayed. By contrast, 3DAC-20 material showed the dispersed graphene sheet structure, as shown in figure 2(k), which played a crucial role in the formation of 3D structure. The high-resolution TEM of 3DAC-20 (figure 2(l))

**Table 1.** Adsorption parameters and the electrical conductivities of 3DAC samples.

Sample	BET SSA (m <sup>2</sup> g <sup>-1</sup> )	Total pore volume (cm <sup>3</sup> g <sup>-1</sup> )	Micropore volume (cm <sup>3</sup> g <sup>-1</sup> )	Mesopore volume (cm <sup>3</sup> g <sup>-1</sup> )	Macropore volume (cm <sup>3</sup> g <sup>-1</sup> )	Ratio of meso- and macro-pores (%)	Electrical conductivity (S m <sup>-1</sup> )
3DAC-15	2044	1.03	0.43	0.58	0.01	56.8	47.5
3DAC-20	2318	1.32	0.49	0.68	0.15	63.2	46.6
3DAC-25	2580	1.22	0.62	0.58	0.03	49.4	40.4

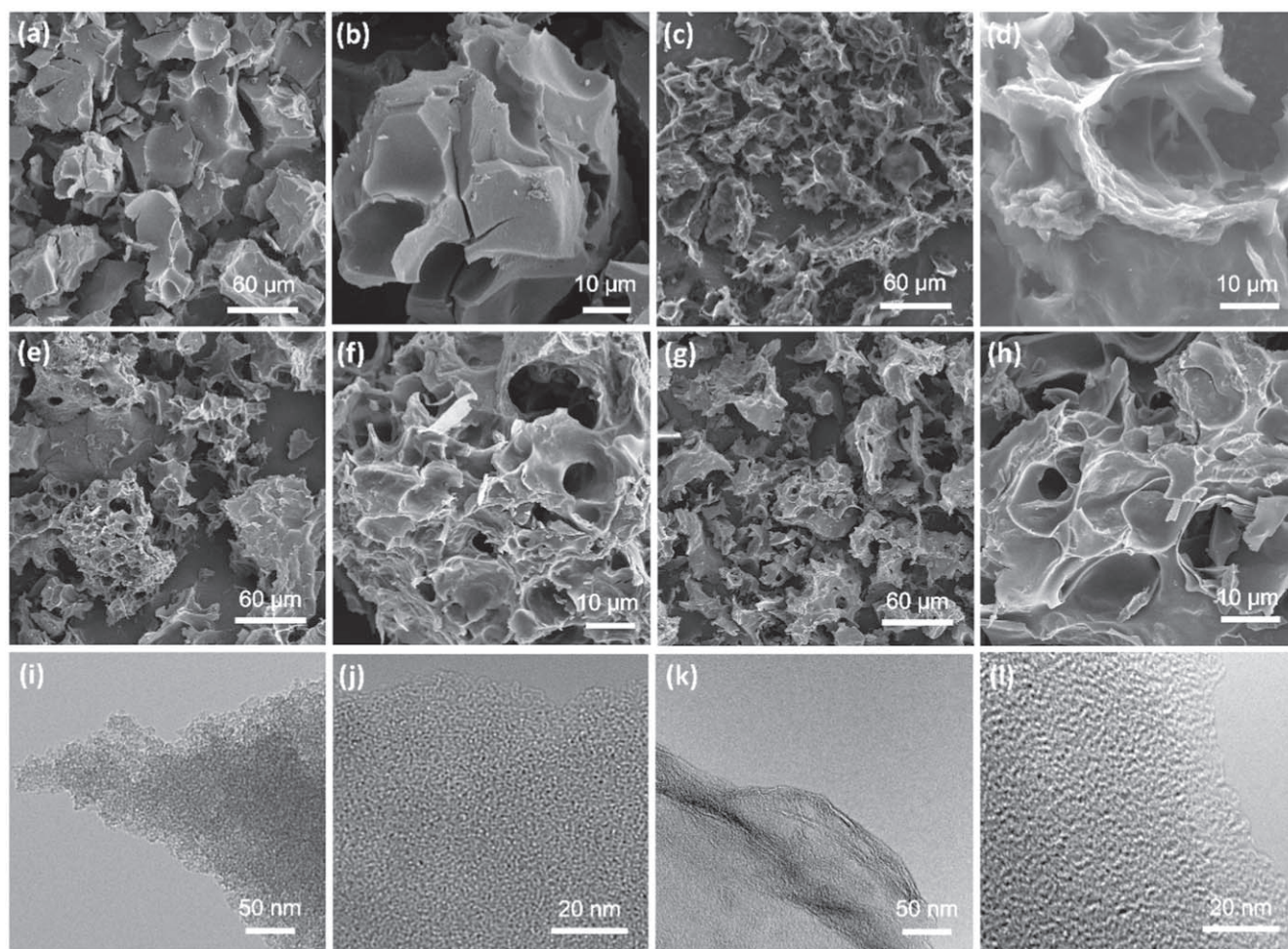


**Figure 2.** SEM and TEM images of series of 3DAC materials. (a), (b) Low magnification and high-resolution SEM images of 3DAC-0. (c), (d) Low magnification and high-resolution SEM images of 3DAC-20. (e), (f) Low magnification and high-resolution SEM images of 3DAC-15. (g), (h) Low magnification and high-resolution SEM images of 3DAC-25. (i), (j) TEM and high-resolution TEM images of 3DAC-0. (k), (l) TEM and high-resolution TEM images of 3DAC-20.

exhibited the micro-/meso- pores distributed throughout the carbon matrix, which formed in the evaporation process of activation agent which left void space [18]. This 3D interconnected porous structures of 3DACs, accompanied by a high ratio of meso-/macro-pores, can provide impressive pathways for the transport and diffusion of electrolyte ions, and thus leading to a high electrochemical performance for SCs. As one of the series of material, 3DAC-15 and 3DAC-25 also presented the similar TEM structures as 3DAC-20 sample, as shown in figure S3.

The structures of 3DAC-20 and the control samples were further evaluated by XRD, Raman and XPS analyses. The XRD pattern in figure 3(a) showed two typical peaks around  $25^\circ$  and  $42^\circ$ , belonging to the (002) and (100) planes of carbon [39, 40]. According to the broad (002) diffraction peak at  $2\theta = 25^\circ$ , the plane interlayer distance of  $\sim 0.36$  nm for the series of samples was shown, indicating a loosened layered structures. The  $c$ -axis height ( $L_c$ ) of the carbon domains is 0.78–1.04 nm calculated by Scherrer equation, being similar to 2–3 layer-stacked graphene sheets [23]. The structural characteristic of 3DAC was further evaluated through Raman spectroscopy. In figure 3(b), the D and G characteristic peaks

centered at  $1346\text{ cm}^{-1}$  and  $1586\text{ cm}^{-1}$  were exhibited, which corresponded to the structural defects and ordered carbon domain structure respectively. The integrated intensity ratio of D to G bands ( $I_D/I_G$ ), is usually used as a measure for the disorder carbon. Among the series of 3DAC samples, 3DAC-0 showed the smallest  $I_D/I_G$  value of 1.46, which can be attributed to the agglomerate structure. By contrast, with the addition and increasing content of GO, the  $I_D/I_G$  values were obviously increased. For 3DAC-20, the value reached to 2.61, supporting a high degree of structural disorder [41, 42]. With further increasing of the GO content, the  $I_D/I_G$  value of 3DAC-15 declined due to the overlap of the more graphene sheets. Based on the Raman results, the mean width ( $L_a$ ) of the carbon domains in 3DAC samples are estimated to about 6.37–11.37 nm, as shown in figure 4(b). Simultaneously, 3DAC-20 sample presented the smallest size of  $\sim 6.37$  nm, indicating the formation of abundant edge parts in 3DAC-20 and thus contributing to a high SSA [13, 15]. For the surface chemical composition analysis of 3DAC-20 and the control samples, XPS studies were further employed. Figure 3(c) showed that the typical 3DAC-20 sample material mainly consisted of C element with 97.44 at%, together with small



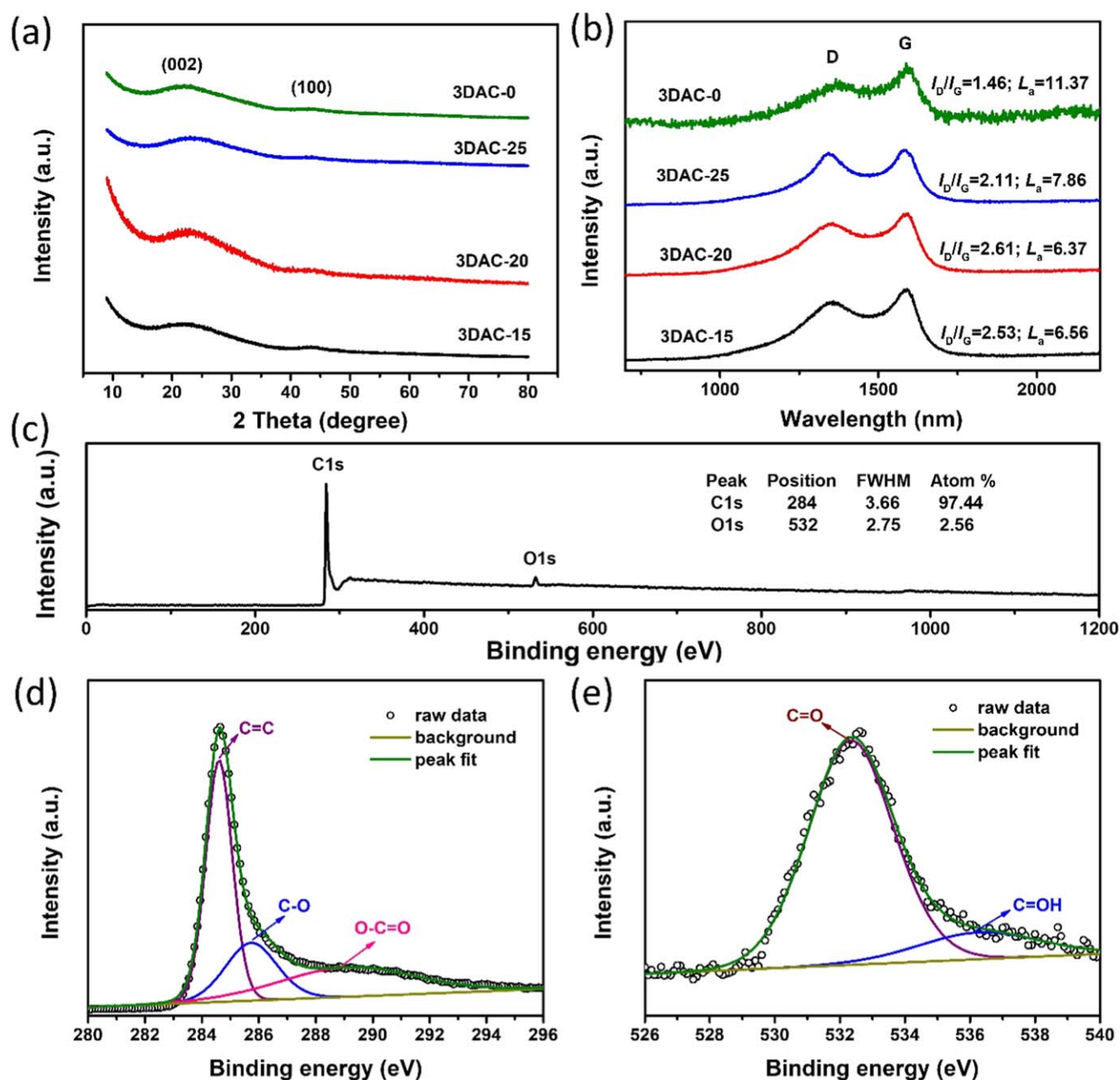


**Figure 3.** Structure analysis of 3DAC samples. (a) XRD results. (b) Raman analysis spectrum. (c)–(e) XPS survey and high resolution spectra of C 1s and O 1s for 3DAC-20.

content of O element (2.56 at%). In the HR C 1s spectrum shown in figure 3(d), three individual peaks at 284.6, 285.7 and 289.1 eV can be obtained, belonging to C=C, C–O and O–C=O, respectively [37, 43]. The existence of O was confirmed by the peaks at 532.3 and 536.2 eV in the O 1s spectrum shown in figure 3(e) [44, 45]. The similar characterization results for the other control samples were obtained, as shown in figures S4–S6.

### 3.2. Electrochemical performance

With its impressive meso-/macro-porous structure and high accessible/effective SSA based on the above microstructure analysis, the electrochemical performance of the 3DAC-20

sample was thus investigated using as the electrode material for EDLC [32]. Figure 4 show the capacitive performance of 3DAC-20 and the control samples for SCs in TEABF<sub>4</sub>/AN organic electrolyte. The CV measurements of 3DAC-20 material were conducted at the scan rates of 10, 20, 50 and 100 mV s<sup>−1</sup>, and the results were shown in figure 4(a). The neat rectangular CV curves suggest an ideal EDLC behavior with fast charge–discharge processes [32]. Moreover, when the scan rate increase to 100 mV s<sup>−1</sup>, the shape of the CV curve was still kept nearly perfectly rectangular, confirming the excellent capacitance response even during the high charge–discharge process. The galvanostatic charge–discharge tests were simultaneously performed at the current densities of 0.5, 1, 2, 5 and 10 A g<sup>−1</sup> to further study the



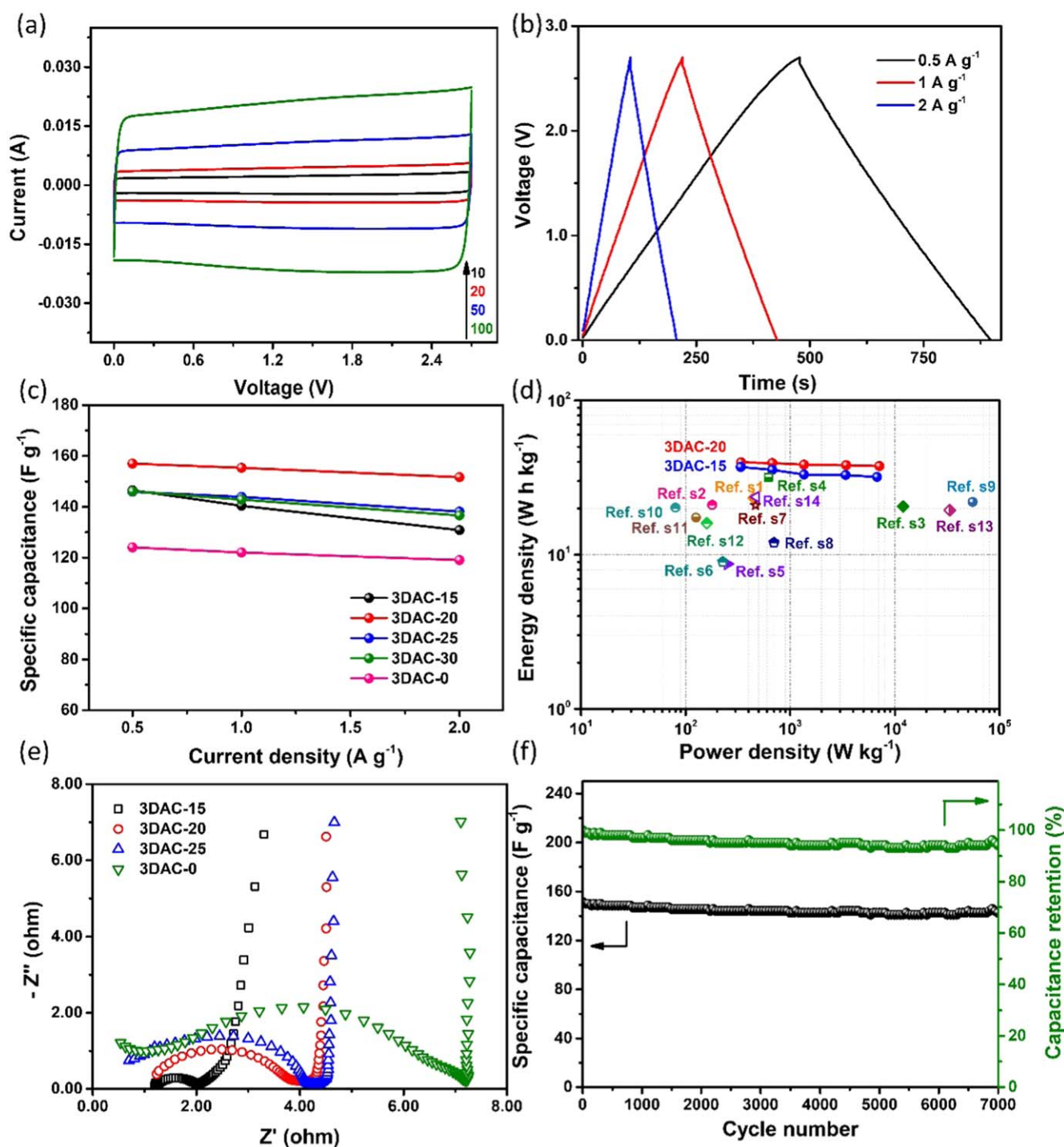


**Figure 4.** Electrochemical performance of prepared 3DAC materials for symmetric SCs in TEABF<sub>4</sub>/AN organic electrolyte. (a) CV results of 3DAC-20 electrode material at the scan rates of 10, 20, 50 and 100 mV s<sup>-1</sup> with the potential range of 0–2.7 V. (b) Galvanostatic charge–discharge test results for 3DAC-20 electrode material at current densities of 0.5, 1 and 2 A g<sup>-1</sup>. (c) Rate performances of 3DAC-20 and the control samples of 3DAC-15, 3DAC-25, 3DAC-30 and 3DAC-0 electrode materials at current densities of 0.5, 1 and 2 A g<sup>-1</sup>. (d) Ragone plots of 3DAC-20 and the control samples including 3DAC-15 and the reported carbon materials. (e) Nyquist plots of 3DAC-20 electrode material and the control samples of 3DAC-0, 3DAC-15 and 3DAC-25 based SCs. (f) Cycling life for 3DAC-20 electrode material after 7000 cycles, tested at a current density of 1 A g<sup>-1</sup> in the potential range of 0–2.7 V.

capacitive performance of the 3DAC-20 sample. As shown in figures 4(b) and S6–S7, the linear symmetric triangle shape charging/discharging profiles demonstrated a fully reversible EDLC's capacitive characteristic in accordance with the CV results. The slight IR-Drop appeared at the early stage of the

discharge process at all tested current densities manifested a small resistance, which will be further discussed in the following EIS studies. Based on the galvanostatic charge–discharge results, the specific capacitance at the series of current densities of 3DAC-20 and the control samples were

calculated, as shown in figure 4(c). Clearly, 3DAC-20 sample with the superior microstructure delivered higher capacitance, along with excellent rate performance. 3DAC-20 sample showed a specific capacitance of  $157 \text{ F g}^{-1}$  at the current density of  $0.5 \text{ A g}^{-1}$ , significantly superior than that of 3DAC-0 ( $124 \text{ F g}^{-1}$ ), 3DAC-15 ( $147 \text{ F g}^{-1}$ ) and 3DAC-25 ( $146 \text{ F g}^{-1}$ ) samples and comparable to the value ( $186 \text{ F g}^{-1}$ ) of all GO derived electrode material using the same preparation method [33]. The enhanced specific capacitance of 3DAC-20 sample can be attribute to the higher ratio of meso-/macro-pores and the corresponding larger meso-/macro-porous volume, which contributed abundant accessible active sites for the electrolyte ions. Furthermore, the microstructure of the electrode materials also are associated with the rate performance, which is another crucial performance parameter of SCs. As expected, the 3DAC-20 sample, with optimum meso-/macro-porous structures benefited to rapidly transport for electrolyte ions and quickly electrical double layer formation, demonstrated the best rate performance. As the current density changed from  $0.5$  to  $2 \text{ A g}^{-1}$ , the specific capacitance was kept at 96.6% better than that of 3DAC-0 (96.0%), 3DAC-15 (89.3%) and 3DAC-25 (94.6%) samples. Even more, the 3DAC-20 electrode materials even retained 94.6% of its original capacitance with  $148.5 \text{ F g}^{-1}$  when the current density enhanced to  $10 \text{ A g}^{-1}$  (figures S7 and S8). Overall, 3DAC-20 sample delivered a superior specific energy density of  $39.7 \text{ W h kg}^{-1}$  with a specific power density of  $340 \text{ W kg}^{-1}$ , showing a higher value than the control sample of 3DAC-15 ( $37.1 \text{ W h kg}^{-1}$  at  $338 \text{ W kg}^{-1}$ ) and other reported carbon materials (table S1). Ragone plots of the 3DAC electrode materials were displayed in figure 4(d). Moreover, with the current density reached to  $10 \text{ A g}^{-1}$  and a power density of  $7.1 \text{ kW kg}^{-1}$  was obtained, the 3DAC-20 electrode material still retains an energy density of  $37.6 \text{ W h kg}^{-1}$ , indicative of a good rate capability.

EIS investigation from  $100 \text{ kHz}$  to  $10 \text{ mHz}$  were conducted to study the ion diffusion behavior and charge transfer resistance of the 3DAC-20 electrode material and the control samples. As shown in figure 4(e), the Nyquist plots of the materials exhibited excellent electrical characteristic, including a straight line at the low frequency region, a straight Warburg line with  $45^\circ$  slope at the middle frequency region and a semicircle shape at the high frequency region [38]. The 3DAC-20 electrode material delivered much smaller size semicircle than that of 3DAC-0, as well as 3DAC-25 sample, showing a lower ion charge transfer resistance at the electrode/electrolyte interface [46, 47]. It is noted that 3DAC-15 shows the smallest size semicircle, which can be contributed to the highest graphene content and the enhanced electrical conductivity. The oblique lines in the low frequency region of the electrode materials were obtained, indicative of a diffusion controlled double layer charge storage process. The steep slope of 3DAC materials based plot suggests a better capacitive behavior [32]. Simultaneously, the short Warburg lines at the  $45^\circ$  portion represent a lower ion diffusion resistance in the electrode [33]. These excellent EIS results for 3DAC materials, especially for 3DAC-20, should come from its 3D interconnected conductive structure and dominant

meso-/macro-pores. The cyclic life of the 3DAC-20 material in TEABF<sub>4</sub>/AN organic electrolyte was further evaluated through the galvanostatic charge–discharge studies at a current density of  $1 \text{ A g}^{-1}$ . As shown in figure 4(f), after 7000 cycles, the 3DAC-20 electrode material presented a capacitance retention ratio of  $\sim 94\%$ , demonstrating an excellent cycling stability.

As discussed above, the outstanding electrochemical performance of the 3DAC-20 electrode material is assigned to its unique microstructures. The 3D connected networks constructed by rGO sheets support the abundant macropores for the fast transport and diffusion of electrolyte ions and electrons. The mesopores produced in the KOH activation process offers sufficient active sites being beneficial to the formation of electrical double layer for electrolyte ions. Thus, the 3D meso-/macro-porous structure contributes the large accessible/effective SSA, excellent electrical conductivity from the networked carbons, efficiently taking advantage of the inner pore's SSA, together with the considerably enhanced ion transport based on the short diffusion lengths between the carbon layers. Thus, it results in remarkably promoted electrochemical performance [43].

#### 4. Conclusions

Using an easily accessible carbon source and GO as precursors, a 3D interconnected porous AC material with controlled meso-/macro-pore structure was prepared through controlling the GO content and the reaction conditions. By controlling such microstructure/morphology, an optimized 3DAC-20 material was obtained and delivers the best capacitive performance in TEABF<sub>4</sub>/AN organic electrolyte system than other controlled samples, in accordance with the specific energy and power density, together with excellent cycling life-time performance. These results demonstrates that by carefully optimizing the precursors and preparation process, the morphology and microstructure of the obtained carbon based materials, such as ACs, could be controlled and optimized for high performance SC electrode materials.

#### Acknowledgments

The authors gratefully acknowledge the financial support from the National Natural Science Foundation of China (NSFC, 51502125), the Natural Science Foundation of Hebei Province of China (E2020408004, B2019408018, B2017408042, E2016408035), Hebei Talent Engineering Training Support Project (A201901064), Key Laboratory of Functional Polymer Materials (Nankai University) of Ministry of Education, the Excellent Going Abroad Experts Training Program in Hebei Province, the Fundamental Research Funds for the Universities in Hebei Province (JYT201901, JYQ201902), the Research Project of Hebei Education Department of China (BJ2016044), the Doctor Fund of Langfang Normal University (LSLB201401), the Hebei Higher Education Teaching Reform Research and Practice Project (2019GJJG357) and the Undergraduate

Innovation and Entrepreneurship Training Program of Hebei Province (S202010100011).

## ORCID iDs

Yanhong Lu  <https://orcid.org/0000-0003-3059-5589>

## References

- [1] Dong X, Jin H, Wang R, Zhang J, Feng X, Yan C, Chen S, Wang S, Wang J and Lu J 2018 High volumetric capacitance, ultralong life supercapacitors enabled by waxberry-derived hierarchical porous carbon materials *Adv. Energy Mater.* **8** 1702695
- [2] Ghosh A and Lee Y H 2012 Carbon-based electrochemical capacitors *ChemSusChem* **5** 480–99
- [3] Vlad A and Balducci A 2017 Supercapacitors: porous materials get energized *Nat. Mater.* **16** 161–2
- [4] Bonaccorso F, Colombo L, Yu G, Stoller M, Tozzini V, Ferrari A C, Ruoff R S and Pellegrini V 2015 Graphene, related two-dimensional crystals, and hybrid systems for energy conversion and storage *Science* **347** 1246501
- [5] Divyashree A, Manaf S, Yallappa S, Chaitra K, Kathyayini N and Hegde G 2016 Low cost, high performance supercapacitor electrode using coconut wastes: eco-friendly approach *J. Energy Chem.* **25** 880–7
- [6] Li L, Hu H, Ding S, Yan X and Wang C 2019 CoNi<sub>2</sub>S<sub>4</sub> nanosheets on nitrogen-doped carbon foam as binder-free and flexible electrodes for high-performance asymmetric supercapacitors *Nanotechnology* **30** 495404
- [7] Niu J, Shao R, Liang J, Dou M, Li Z, Huang Y and Wang F 2017 Biomass-derived mesopore-dominant porous carbons with large specific surface area and high defect density as high performance electrode materials for Li-ion batteries and supercapacitors *Nano Energy* **36** 322–30
- [8] Lu Y, Huang Y, Zhang M and Chen Y 2014 Nitrogen-doped graphene materials for supercapacitor applications *J. Nanosci. Nanotechnol.* **14** 1134–44
- [9] Huang Y, Liang J and Chen Y 2012 An overview of the applications of graphene-based materials in supercapacitors *Small* **8** 1805–34
- [10] Chaitra K, Vinny R T, Sivaraman P, Reddy N, Hu C Y, Venkatesh K, Vivek C S, Nagaraju N and Kathyayini N 2017 KOH activated carbon derived from biomass-banana fibers as an efficient negative electrode in high performance asymmetric supercapacitor *J. Energy Chem.* **26** 56–62
- [11] Xiao M, Su Y, Zhao M and Du B 2020 Synthesis of CoTe nanowires: a new electrode material for supercapacitor with high stability and high performance *Nanotechnology* **31** 055706
- [12] Zhang L *et al* 2013 Controlling the effective surface area and pore size distribution of sp<sup>2</sup> carbon materials and their impact on the capacitance performance of these materials *J. Am. Chem. Soc.* **135** 5921–9
- [13] Lu Y, Long G, Zhang L, Zhang T, Zhang M, Zhang F, Yang Y, Ma Y and Chen Y 2016 What are the practical limits for the specific surface area and capacitance of bulk sp<sup>2</sup> carbon materials? *Sci. China Chem.* **59** 225–30
- [14] Ma C, Liu X, Min J, Li J, Gong J, Wen X, Chen X, Tang T and Mijowska E 2020 Sustainable recycling of waste polystyrene into hierarchical porous carbon nanosheets with potential applications in supercapacitors *Nanotechnology* **31** 035402
- [15] Zhang L *et al* 2013 Porous 3D graphene-based bulk materials with exceptional high surface area and excellent conductivity for supercapacitors *Sci. Rep.* **3** 1408
- [16] Ling Z, Wang Z, Zhang M, Yu C, Wang G, Dong Y, Liu S, Wang Y and Qiu J 2016 Sustainable synthesis and assembly of biomass-derived B/N co-doped carbon nanosheets with ultrahigh aspect ratio for high-performance supercapacitors *Adv. Funct. Mater.* **26** 111–9
- [17] Hao Z-Q, Cao J-P, Wu Y, Zhao X-Y, Zhuang Q-Q, Wang X Y and Wei X-Y 2017 Preparation of porous carbon sphere from waste sugar solution for electric double-layer capacitor *J. Power Sources* **361** 249–58
- [18] Lu Y *et al* 2017 Mesoporous activated carbon materials with ultrahigh mesopore volume and effective specific surface area for high performance supercapacitors *Carbon* **124** 64–71
- [19] Dutta S, Bhaumik A and Wu K C W 2014 Hierarchically porous carbon derived from polymers and biomass: effect of interconnected pores on energy applications *Energy Environ. Sci.* **7** 3574–92
- [20] Wang D-W, Li F, Liu M, Lu G Q and Cheng H-M 2008 3D aperiodic hierarchical porous graphitic carbon material for high-rate electrochemical capacitive energy storage *Angew. Chem., Int. Ed.* **47** 373–6
- [21] Wang H *et al* 2013 Interconnected carbon nanosheets derived from hemp for ultrafast supercapacitors with high energy *ACS Nano* **7** 5131–41
- [22] Long C, Jiang L, Wu X, Jiang Y, Yang D, Wang C, Wei T and Fan Z 2015 Facile synthesis of functionalized porous carbon with three-dimensional interconnected pore structure for high volumetric performance supercapacitors *Carbon* **93** 412–20
- [23] Yao Y *et al* 2018 Unlocking the potential of graphene for water oxidation using an orbital hybridization strategy *Energy Environ. Sci.* **11** 407–16
- [24] Guo D, Xin R, Wang Y, Jiang W, Gao Q, Hu G and Fan M 2019 N-doped carbons with hierarchically micro- and mesoporous structure derived from sawdust for high performance supercapacitors *Microporous Mesoporous Mater.* **279** 323–33
- [25] Jia H, Sun J, Xie X, Yin K and Sun L 2019 Cicada slough-derived heteroatom incorporated porous carbon for supercapacitor: ultra-high gravimetric capacitance *Carbon* **143** 309–17
- [26] Wang C, Wang J, Wu W, Qian J, Song S and Yue Z 2019 Feasibility of activated carbon derived from anaerobic digester residues for supercapacitors *J. Power Sources* **412** 683–8
- [27] Wu Y, Yi N, Huang L, Zhang T, Fang S, Chang H, Li N, Oh J, Lee J A and Kozlov M 2015 Three-dimensionally bonded spongy graphene material with super compressive elasticity and near-zero Poisson's ratio *Nat. Commun.* **6** 6141
- [28] Lu Y, Ma Y, Zhang T, Yang Y, Wei L and Chen Y 2018 Monolithic 3D cross-linked polymeric graphene materials and the likes: preparation and their redox catalytic applications *J. Am. Chem. Soc.* **140** 11538–50
- [29] Chen W, Xiao P, Chen H, Zhang H, Zhang Q and Chen Y 2019 Polymeric graphene bulk materials with a 3D cross-linked monolithic graphene network *Adv. Mater.* **31** 1802403
- [30] Lu Y *et al* 2016 Photoprompted hot electrons from bulk cross-linked graphene materials and their efficient catalysis for atmospheric ammonia synthesis *ACS Nano* **10** 10507–15
- [31] Lu Y *et al* 2017 High activity of hot electrons from bulk 3D graphene materials for efficient photocatalytic hydrogen production *Nano Res.* **10** 1662–72
- [32] Wang Y, Shi Z, Huang Y, Ma Y, Wang C, Chen M and Chen Y 2009 Supercapacitor devices based on graphene materials *J. Phys. Chem. C* **113** 13103–7

- [33] Lu Y, Zhang F, Zhang T, Leng K, Zhang L, Yang X, Ma Y, Huang Y, Zhang M and Chen Y 2013 Synthesis and supercapacitor performance studies of N-doped graphene materials using o-phenylenediamine as the double-N precursor *Carbon* **63** 508–16
- [34] Zhang M, Sun Z, Zhang T, Qin B, Sui D, Xie Y, Ma Y and Chen Y 2017 Porous asphalt/graphene composite for supercapacitors with high energy density at superior power density without added conducting materials *J. Mater. Chem. A* **5** 21757–64
- [35] Zhang F, Zhang T, Yang X, Zhang L, Leng K, Huang Y and Chen Y 2013 A high-performance supercapacitor-battery hybrid energy storage device based on graphene-enhanced electrode materials with ultrahigh energy density *Energy Environ. Sci.* **6** 1623
- [36] Bi H, Xie X, Yin K, Zhou Y, Wan S, He L, Xu F, Banhart F, Sun L and Ruoff R S 2012 Spongy graphene as a highly efficient and recyclable sorbent for oils and organic solvents *Adv. Funct. Mater.* **22** 4421–5
- [37] Feng W, He P, Ding S, Zhang G, He M, Dong F, Wen J, Du L and Liu M 2016 Oxygen-doped activated carbons derived from three kinds of biomass: preparation, characterization and performance as electrode materials for supercapacitors *RSC Adv.* **6** 5949–56
- [38] Zhu Y, Chen M, Zhang Y, Zhao W and Wang C 2018 A biomass-derived nitrogen-doped porous carbon for high-energy supercapacitor *Carbon* **140** 404–12
- [39] Sun J, Niu J, Liu M, Ji J, Dou M and Wang F 2018 Biomass-derived nitrogen-doped porous carbons with tailored hierarchical porosity and high specific surface area for high energy and power density supercapacitors *Appl. Surf. Sci.* **427** 807–13
- [40] Lian J, Cheng R, Xiong L, Pang D, Tian X, Lei J, He R, Yu X, Duan T and Zhu W 2019 Supercapacitors with high nitrogen content by cage-like *Ganoderma lucidum* spore *Appl. Surf. Sci.* **494** 230–8
- [41] Gopiraman M, Deng D, Kim B-S, Chung I-M and Kim I S 2017 Three-dimensional cheese-like carbon nanoarchitecture with tremendous surface area and pore construction derived from corn as superior electrode materials for supercapacitors *Appl. Surf. Sci.* **409** 52–9
- [42] Wei L, Sevilla M, Fuertes A B, Mokaya R and Yushin G 2012 Polypyrrole-derived activated carbons for high-performance electrical double-layer capacitors with ionic liquid electrolyte *Adv. Funct. Mater.* **22** 827–34
- [43] Lu S-Y, Jin M, Zhang Y, Niu Y-B, Gao J-C and Li C M 2018 Chemically exfoliating biomass into a graphene-like porous active carbon with rational pore structure, good conductivity, and large surface area for high-performance supercapacitors *Adv. Energy Mater.* **8** 1702545
- [44] Bai Q, Xiong Q, Li C, Shen Y and Uyama H 2018 Hierarchical porous carbons from a sodium alginate/bacterial cellulose composite for high-performance supercapacitor electrodes *Appl. Surf. Sci.* **455** 795–807
- [45] Zhang Y, Wang F, Zhu H, Zhou L, Zheng X, Li X, Chen Z, Wang Y, Zhang D and Pan D 2017 Preparation of nitrogen-doped biomass-derived carbon nanofibers/graphene aerogel as a binder-free electrode for high performance supercapacitors *Appl. Surf. Sci.* **426** 99–106
- [46] Sui D, Xie Y, Zhao W, Zhang H, Zhou Y, Qin X, Ma Y, Yang Y and Chen Y 2018 A high-performance ternary Si composite anode material with crystal graphite core and amorphous carbon shell *J. Power Sources* **384** 328–33
- [47] Sui D, Xu L, Zhang H, Sun Z, Kan B, Ma Y and Chen Y 2020 A 3D cross-linked graphene-based honeycomb carbon composite with excellent confinement effect of organic cathode material for lithium-ion batteries *Carbon* **157** 656–62